Journal of Materials Chemistry A

Accepted Manuscript

ROYAL SOCIETY OF CHEMISTRY

www.rsc.org/materialsA

One-pot Construction of Three Dimensional $CoMoO_4/Co_3O_4$ Hybrid Nanostructures and Their Application in Supercapacitors

Min Zhou, Fei Lu, Xiaoshuang Shen, Weiwei Xia, Hui He and Xianghua Zeng[*]

College of Physical Science and Technology, and Institute of Optoelectronic Technology, Yangzhou University, Yangzhou 225002, People's Republic of China

ABSTRACT

A facile one-pot hydrothermal method is developed to synthesize $CoMoO_4/Co_3O_4$ hybrid nanostructure, in which the $CoMoO_4$ nanosheets are supported by the hierarchical framework assembled by Co_3O_4 nanorods. The morphology and structure of this three dimensional nanocomposite were characterized in detail, based on which a rational growth mechanism was proposed. The unique structure features of our $CoMoO_4/Co_3O_4$ hierarchical nanohybrid allow for high specific surface and multiple Faradaic redox reactions for electrode materials of supercapacitors. Consequently, a high specific capacitance (1062.5 F/g at the current density of 1 A/g) and an excellent cyclic performance (90.38% of the initial capacitance retained after 2000 cycles at a current density of 20 A/g) were obtained. Besides, asymmetric supercapacitor with high energy density of 31.64 Wh/kg is achieved at the power density of 7270 W/kg. This work thus provids an excellent candidate for high-performance supercapacitor fabrication.

KEYWORDS

Hybrid material, hierarchical structure, growth mechanism, supercapacitor

1. INTRODUCTION

Electrochemical energy storage devices have attracted much attention by storing energy from the entire energy system while releasing it when in demand, which are expected to play key roles in the utilization of renewable energy. Among these devices, supercapacitors are of great interests because they filled the gap between high energy density from batteries and high power density from traditional capacitors. [1-3] The performance of a supercapacitor is generally determined by the specific capacitance, other factors also profoundly affect the applicability of the material as a supercapacitor electrode. For instance, low cost, cyclic durability and facile synthetic route are desirable for practical applications. [4, 5] Although RuO_2 displayed favorable specific capacitance and cyclic durability as supercapacitor electrode material, it is not suitable for commercialization because of the high cost of ruthenium. [6, 7] Other transition-metal oxides, such as MnO_2, NiO and Co_3O_4, possess remarkable theoretical specific capacitance and low cost, but suffer from their poor conductivity and durability. [8-12] Thus, it is imperative to develop a low cost and readily-prepared electrode for supercapacitors with high specific capacitance and cyclic durability.

It is known that the enhancements of carrier transport ability and specific surface area of electrode materials, are two effective routes to improve the pseudocapacitance of electrode materials.[13-16] Recently, binary metal oxides exhibit excellent electrochemical performance for providing multiple redox reactions and high electrical conductivity. Molybdates, including $CoMoO_4$, $MnMoO_4$ and $NiMoO_4$, have demonstrated their potentials in this area. [14, 16-19] Liu et al. synthesized $CoMoO_4$

nanorods via hydrothermal method, which exhibited a specific capacitance of 286 F/g at the current density of 5 mA/cm^2, and 97.5% of the initial capacitance retained after 2000 cycles. [17] Mai and co-workers investigated the supercapacitor performance of CoMoO4/MnMoO4 nanocoposites, the specific capacitance of which is 187.1 F/g at current density of 1 A/g. [18] Minakshi and co-worker found the $CoMoO_4$ nanosheets modified with chitosan, comparing with the chitosan free $CoMoO_4$, displayed enhanced supercapacitor performance in NaOH electrolyte. [20] To make further improvement on the electrochemical performance, various nanomaterials were introduced into molybdates to enhance the specific surface areas of the electrode materials. For instance, Xia et al. obtained a specific capacitance of 394.5 F/g from $CoMoO_4$/graphene composites at the scan rate of 1 mV/s. [16] Besides, hierarchical Co_3O_4@$CoMoO_4$ core/shell nanowire arrays grown on nickel foam were fabricated by Gu and co-workers via a ion exchange hydrothermal method, which exhibit a specific capacitance of 1040 F/g at a current density of 1 A g^{-1}. [21] It is expected that this integrating approach can be potentially adopted to widely prepare supercapacitor electrode materials with better performance. However, the reported strategies toward molybdates composites generally need two or more steps in preparation. A more facile method therefore is desirable to meet the low cost requirement in the supercapacitors application.

In this study, we present hierarchical $CoMoO_4$/Co_3O_4 hybrid nanostructures as electrode material for supercapacitors, in which the $CoMoO_4$ nanosheets are supported by Co_3O_4 nanorods framework. Different from previous reported

$CoMoO_4/Co_3O_4$ and other $CoMoO_4$ based composites, which need an additional ion exchange process in preparation, this unique nanocomposite is synthesized via a facile one-pot hydrothermal method and a subsequent heating treatment. Furthermore, in addition to the favorable electric conductivity from $CoMoO_4$, this hybrid nanostructure is of high specific surface area due to their porosity and three dimensional features. The electrochemical tests reveal that the as-prepared 3D hybrid structure provides excellent specific capacitance and cyclic stability at high current density, indicating the potential of alternative electrode material in supercapacitors.

2. EXPERIMENTAL SECTION

2.1 Synthesis. All chemicals were of analytical grade and were used without further purification. The precursor of the hierarchical $CoMoO_4/Co_3O_4$ nanocomposite was synthesized by a one-pot hydrothermal method. Briefly, 1 mmol $Co(NO_3)_2$, 1 mmol Na_2MoO_4 and 7.5 mmol urea were dissolved in 20 mL distilled water, the solution then was transformed into a 46 ml Teflon-lined stainless steel autoclave and kept at 150 ^oC for 2 h. To investigate the growth mechanism, the time dependent products were obtained by terminating the reaction at 30 min, 60 min and 90 min, respectively. The precipitates were washed with distilled water and ethanol several times, respectively, and vacuum dried at 60 ^oC for 8 h. The contrast experiment was carried out by adjusting the concentration of cobalt and molybdenum salts as 2:1 labeled as sample S21 and 1:2 labeled as sample S12 with other conditions unchanged and the sample S11 represents the ratio of 1:1. The all as-prepared precursors were then calcined at 500 ^oC for 3 h with a heating rate of 1 ^oC/min to obtain the annealed

sample.

2.2 Characterization. The crystal phase of the as synthesized samples was characterized by X-ray Diffraction (XRD with monochromatized Cu Ka irradiation) with Shimadzu XRD-7000 diffraction instrument. The morphology and microstructure of the synthesized nanomaterials were investigated by scanning electron microscope (SEM, Hitachi S4800), transmission electron microscope (TEM, Tecnai 12) and high resolution transmission microscope (HRTEM, Tecnai G2 F30 S-TWIN with the accelerating voltage of 300 kV). Fourier transform infrared spectra (FTIR) and Raman spectroscopy were detected on Varian 610/670-IR microscope and Renishaw inVia microscope. The nitrogen absorption-desorption isotherm was measured using Brunauer–Emmett–Teller (BET) theory with a surface area analyzer (BeiShiDe, 3H-2000PM2). The pore size distribution was conducted using Barrett-Joyner-Halenda (BJH) model.

2.3 Electrochemical Measurements. The electrochemical measurements were carried out in a three-electrode electrochemical cell containing 3 M KOH aqueous solution as electrolyte, the Pt foil served as the counter electrode and the saturated calomel electrode (SCE) acted as the reference electrode. The working electrode is consisted of active material (the as synthesized $CoMoO_4/Co_3O_4$), conductive graphite and PTFE with the mass ratio of 80:15:5. The slurry was pasted onto the Ni foam and vacuum dried overnight. Cyclic Voltammetry and galvanostatic charge-discharge investigation were carried out using a CHI660E electrochemical workstation (Huake, Beijing). The specific capacitance (F/g) of the electrode was calculated from

galvanostatic charge-discharge (GCD) curves. Electrochemical impedance spectroscopy (EIS) measurements were detected with AC amplitude of 5 mV in a frequency range of 100 KHz to 0.01 Hz. The mass of active material in working electrode is 2.1 mg/cm^2.

For the fabrication of asymmetric supercapacitor, the previous working electrode served as the positive electrode, and the preparation of negative electrode utilizing activated carbon (AC) followed the same route of positive electrode. The two electrodes and a separator combined with 3 M KOH as the electrolyte to assemble the full cell. The mass loading of the positive and negative materials were 2.5 and 5.9 mg/cm^2.

RESULTS AND DISCUSSION

3.1 Morphology and structure characterization. The morphology and microstructure of the samples were investigated by SEM and TEM, as shown in Fig 1. In Fig 1a, flower-like microspheres consisted of nanosheets are observed from the precursor. The average diameter of these microspheres is about 4 μm, while the thickness of the nanosheets is about 10 - 20 nm, as displayed in the inset of Fig 1a. Fig 1b indicates that the hierarchical morphology still remains after the sample annealed at 500 ^{o}C. Nevertheless, the smooth surface of the sample has turned to granular ones after annealing, implying the remerging and growing of the crystals during this process. [22] TEM measurements were carried out to further investigate the structure of the samples. Interestingly, Fig 1c reveals that the hierarchical microspheres are constructed with nanorod-assembled framework inside and

interlaced nanosheets outside, in which the nanosheets are supported by the nanorods backbone. The diameter and length of the nanorod are about dozens nanometers and hundreds nanometers, respectively. The annealed sample still remains the hierarchical structure but presents granulated particles with porosities, as shown in Fig 1d, which is in quite accordance with the results of SEM images.

XRD measurement was conducted to determine the phase structure of the products. The XRD pattern of the annealed sample in Fig 2a presents two sets of peaks, which are indexed to $CoMoO_4$ (JCPDS no.21-0868) and Co_3O_4 (JCPDS no.80-1542), respectively. The annealed sample therefore is considered to be a hybrid material of the two phases. For the precursor, most of the diffraction peaks in Fig 2b are attributed to the $Co(CO_3)_{0.5}(OH)\cdot 0.11H_2O$ (JCPDS no.48-0084). Besides, the peak centered at 59 ^{o} is considered to be the diffraction peak from the precursor of $CoMoO_4$. Both the two phases in the precursor were transformed to $CoMoO_4$ and Co_3O_4 during the annealing process. The assignment of the precursor-$CoMoO_4$ is based on the component analysis of the annealed sample in Fig 2a, and the FTIR and Raman spectra from the precursor samples discussed later. An accurate identification of this precursor is still needed in further study.

The hybrid characteristic of the sample is also verified by FTIR spectra. In Fig 2c, the absorption peak at 1000 cm^{-1} in the two patterns is assigned to the bending modes of molecularly chemisorbed water, while the band around 1500 cm^{-1} corresponds to the bending modes of the molecularly chemisorbed water. [22, 23] For the precursor sample, the peaks at 977~921, 829, 680, 473 cm^{-1} correspond to δ(M-OH), δ(CO_3),

ρ(OCO), ρ_w(M-OH) of $Co(CO_3)_{0.5}(OH)\cdot 0.11H_2O$. [24] Furthermore, the peaks at 862, 815 cm^{-1} are assigned to Mo-O-Mo, while the peak at 433 cm^{-1} corresponds to the superposition of MoO and CoO_6 building groups, which are indexed to the precursor of $CoMoO_4$. [25] For the annealed sample, the formation of Co_3O_4 spinel oxide is substantiated by the absorption peaks at 655 and 557 cm^{-1}. [23] The other four peaks at 950, 858, 782 and 418 cm^{-1} demonstrate the formation of $CoMoO_4$. [25, 26]

The structure information of the samples was further studied by Raman spectroscopy. As shown in Fig 2d, the peaks centered at 187, 473, 521, 604, 672 cm^{-1} are corresponding to F_{2g}, E_g, F_{2g}, F_{2g}, A_{1g} models of Co_3O_4, respectively. [27] The other band centered at 938, 895, 360 and 331 cm^{-1} are for the stretching vibration of Co-O-Mo in $CoMoO_4$. [18, 28] For the Raman spectrum of the precursor in Fig 2e, the peaks labeled as pre-$CoMoO_4$ are attributed to the characterization of α-$CoMoO_4$, [29] while the peaks located at 440 cm^{-1} comes from symmetric stretching (Ag) model vibration of Co-O and the symmetric vibration of Co-OH ($A_{1g(T)}$) accounts for the peak of 521 cm^{-1}. [30] The existence of $CoMoO_4$ precursor confirmed by FTIR and Raman spectra is consistence to the phase structure of the precursor we proposed above.

The specific surface area of the samples is another key parameter related to the electrochemical performance. As shown in Fig 2f and g, the isotherm of both samples present typical Langmuir type Ⅳ and the pores mainly distribute in mesoporous scale. The specific surface area of the precursor and the annealed sample are 94.95 and 59.05 m^2/g, respectively. The decrease of the specific surface area after the

annealing is caused by the crystalline growth and remerging processes during the annealing treatment. [22] Nevertheless, the specific surface area of 59.05 m^2/g from the annealed sample is still larger than those of the molybdates nanomaterials reported previously. [28, 31] A larger specific surface area of the electrode material is helpful to improve the specific capacitance by offering sufficient active sites in the electrolyte.

3.2 Growth mechanism. So far, the precise distribution of the two phases and the forming mechanism of the hybrid nanostructure are not clarified. The time dependent experiments were thus conducted to reveal these issues, as shown in Fig 3. The SEM images exhibit the morphological transformation of the intermediate products with the reaction time varied from 30 to 90 min. The product obtained at 30 min is composed of uniform nanorods with an average diameter of about 300 nm, as shown in Fig 3e. As the reaction time increases to 60 min, the nanorods become smaller with diameters less than 100 nm and gradually self-assemble together as some 3D frameworks, as displayed in Fig 3f. Then, nanosheets are observed grown on the nanorods to form the hierarchical structure in Fig 3g. Meanwhile, XRD measurement was employed to study the phase evolution of the products, as shown in Fig 3i-l. The product with the reaction time of 30 min is indexed to $CoMoO_4$. [31, 32]With the reaction time increased, however, the intensity of the diffraction peaks attributed to $CoMoO_4$ declined, while the diffraction peaks attributed to $Co(CO_3)_{0.5}(OH)\cdot 0.11H_2O$ and precursor of $CoMoO_4$ increased, indicating a phase transformation occurred during this process.

Based on the above observations, the growth mechanism of this unique nanostructure is clarified as follows. Firstly, $CoMoO_4$ nanorods are formed at the

initial stage of the hydrothermal reaction. Nevertheless, the $CoMoO_4$ nanorods are then dissolved, due to the existence of $NH_3 \cdot H_2O$, which is decomposed from urea in the solution. This process is similar to the dissolution of MoO_3 in ammonia, [16, 33-35] as explained in equation (1) and equation (2):

$$CO(NH)_2+H_2O \rightarrow 2NH_3+CO_2 \quad (1)$$

$$2NH_3+2H_2O \rightarrow 2NH_4^{+}+2OH^{-} \quad (2)$$

$$CO_2+H_2O \rightarrow CO_3^{2-}+2H^{+} \quad (3)$$

$$Co^{2+}+OH^{-}+0.5CO_3^{2-}+0.11H_2O \rightarrow Co(CO_3)_{0.5}(OH)\cdot 0.11H_2O \quad (4)$$

Then, the Co^{2+} then combines with OH^- and CO_3^{2-} in the solution, to compound $Co(CO_3)_{0.5}(OH)\cdot 0.11H_2O$ nanorods, followed as the equation (2-4).[36] After that, the nanosheets of the precursor-$CoMoO_4$ grew onto the nanorods, in which the nanorods framework served as backbone of the hierarchical hybrids. The growth process of the hybrid nanostructure is illustrated in Fig 3a-d.

HRTEM measurement was conducted on the annealed sample to further confirm the phase distribution of the hybrid nanostructure. To obtain the crystalline information of the nanorods located in the interior, the sample was ultrasonic treated before testing to destroy the hierarchical nanostructure. Thus, monodispersed Co_3O_4 nanorods and $CoMoO_4$ fragment divorced from the nanosheets are displayed in Fig 4a-c. The interlayer spacings of 0.208, 0.212 nm from the nanosheet in Fig 4b correspond to the (422) and (132) plane of $CoMoO_4$, while the spacing value of 0.202 and 0.234 nm from the nanorod in Fig 4c are attributed to the $(\bar{4}00)$ and (222) plane of Co_3O_4. The HRTEM results demonstrate that the crystalline structures of the nanorods

and nanosheets in the hybrid nanostructure are Co_3O_4 and $CoMoO_4$, respectively, which are consistent with the phase distribution proposed above. The polycrystalline and hybrid nature of the sample is also supported by its SAED analysis illustrated in Fig 4d.

3.3 Electrochemical performance of $CoMoO_4/Co_3O_4$. The supercapacitor performance of the 3D hybrid $CoMoO_4/Co_3O_4$ nanostructure was evaluated in a three-electrode cell with 3 M KOH electrolyte. The representative cyclic voltammetry (CV) curves were presented in Fig 5a with the scan rates varied from 10 to 300 mV/s. The cyclic voltammetry curves obtained under different scan rates show a pair of redox peaks, which are attributed to Faradaic redox reaction, indicating the pseudocapacitive feature of the electrode materials. The pseudocapacitance mainly comes from the Faradaic redox reactions listed as follows: [18]

$$3[Co(OH)_3]^- \Leftrightarrow Co_3O_4 + 4H_2O + OH^- + 2e^- \quad (5)$$

$$Co_3O_4 + H_2O + OH^- \Leftrightarrow 3CoOOH + e^- \quad (6)$$

$$CoOOH + OH^- \Leftrightarrow CoO_2 + H_2O + e^- \quad (7)$$

The anodic peak shifts to higher potential, while the cathodic peak shifts to lower potential as the scanning rate is increased due to the insufficient intercalation of the ions from electrolyte into electrode under faster charge and discharge rates. [37] The peak current increases linearly with the increasing of scanning rate, implies that the electrochemical process in the electrode is mainly surface-controlled. [37] The redox peaks retain ideally even at high scanning rate, indicating the rapid electronic and ionic transport processes, which are beneficial to the charge-discharge performance at

high rate. [38, 39]

To estimate the energy storage performance of the electrode, the specific capacitance was calculated based on the following formula:

$$C = \frac{I_{discharge} \cdot \Delta t}{m \cdot \Delta V} \qquad (8)$$

where C (F/g) is the specific capacitance of the active materials, I (A) is the current applied to charge and discharge, m (g) is the mass of the active material of the electrode, the ΔV (V) and Δt (s) are the dropout voltage and the elapsed time during discharge period, respectively. According to the galvanostatic charge-discharge behavior exhibited in Fig 5b, the specific capacitances of 1062.5, 945, 800, 700 and 635 F/g were calculated from the annealed sample at the current densities of 1, 2, 5, 10, 20 A/g, respectively. The nonlinear discharge curves further verified the pseudocapacitive behavior of the electrode. The cyclic stability is another critical parameter for supercapacitors, which was carried out at a constant current density of 20 A/g. As displayed in Fig 5c, 90.38% of the initial capacitance was maintained after 2000 cycles. Furthermore, the insets in Fig 5c reveal that the curves of charging and discharging time are almost unchanged from the first ten cycles to the last ten cycles, suggesting the high coulombic efficiency and low polarization of the electrode material.[39]

Electrochemical impedance spectra (EIS) measurement was utilized to further investigate the ion diffusion and charge transfer process in the electrode. From Fig 5d, both Nyquist plots obtained before and after the cycles start with a semicircle in the high frequency, and followed with an approximate vertical line in the middle and low

frequency region. Both of the curves in the low frequency region show a straight line with the same gradient along with the imaginary axis, reflecting the fast kinetics of the diffusion process and the low Warburg resistance. [39, 40] In addition, as described in the inset, the internal resistance (R_s), reflected in the intersection point between the Nyquist plots and the real axis, remains almost unchanged after the cycles, suggesting few declination of the conductivity in the electrode during the charging-discharging processes. Moreover, the ideal small semicircle diameter performed in the curves corresponds to the low interfacial charge transfer resistance (R_{ct}), and the smaller semicircle in the curve obtained after the cycles implies gradual infiltration of the electrolyte, the activation of the electrode material, and the improved kinetics of ion diffusion. [8, 41, 42]

The electrochemical properties of the precursor sample were also studied, as shown in Fig 6. According to the GCD curves in Fig 6b, the specific capacitance of 697.8, 610, 562.5, 527, 475 F/g are achieved at 1, 2, 5, 10, 20 A/g, respectively. There is attenuation of the specific capacitance compared with the annealed sample. The cyclic stability of the precursor sample is shown in Fig 6c, which indicates that 93.6% of the initial capacitance is remained after 2000 cycles. The precursor sample exhibits superior cyclic stability than the annealed sample, since the annealing process causes damages to the integrity of the sample. Despite a slight declination in cyclic stability, the annealing process is considered to be necessary to promote the electrochemical performance of the sample.

3.4 Discussions. Our results demonstrate that the 3D $CoMoO_4/Co_3O_4$ hierarchical

nanohybrid electrode offers a large specific capacitance and excellent cyclic stability, providing a promising candidate for the fabrication of high-performance supercapacitors. In our view, the unique nanostructure of the $CoMoO_4/Co_3O_4$ nanohybrid plays a key role in its electrochemical performance. To confirm this, we reset the molar ratio between cobalt and molybdenum salts in the precursor solution to achieve the morphology and structure evolution of the products, as shown in Fig S1. The unique hierarchical nanohybrid studied above was obtained with a molar ratio between Co^{2+} and Mo^{6+} of 1:1. When the molar ratio was changed into 2:1, the products are the $CoMoO_4/Co_3O_4$ nanohybrid and Co_3O_4 nanourchins. While the products are collapsed $CoMoO_4/Co_3O_4$ nanohybrid and $NaCo_{2.31}(MoO_4)_3$ rods, when the molar ratio was tuned to 1:2. Both of the two samples obtained by changing the initial molar ratio displayed inferior electrochemical performance. For a convenient comparison, the CV curves of the three samples at the scanning rate of 100 mV/s are shown in Fig 7a. The area surrounded with the CV curve of sample S11 is obviously larger than those of the other two samples, indicating the better capacitance of the sample. The specific capacitances of different samples are also calculated based on the galvanostatic charge-discharge curves in Fig 7b. The specific capacitance of sample S21 and S12 are 748.8 and 243.5 F/g, respectively, which is inferior to the sample S11. These results demonstrate that an appropriate molar ratio between cobalt and molybdenum salts in the precursor solution is necessary to achieve such an outstanding electrochemical performance. Otherwise, the exceeding of cobalt or molybdenum salts lead to the formation of Co_3O_4 and $NaCo_{2.31}(MoO_4)_3$ rods in the

products, which are inferior to $CoMoO_4/Co_3O_4$ nanostructures as electrode materials.

Based on the experimental results presented above, the excellent electrochemical performance of the $CoMoO_4/Co_3O_4$ nanohybrids benefits from the following facts. First, the vertically grown $CoMoO_4$ sheets offer Faradaic redox reaction of the electrodes with high pseudocapacitive, as proved in previous studies. [16-21] Second, such mesoporosity structure with large specific surface area offers sufficient electron-active sites and transport channels to facilitate more electrochemical reactions in the redox process, resulting in improved specific capacitance. Third, the Co_3O_4 framework in our hierarchical nanohybrid not only improves the specific surface area by serving as the backbone of the nanostructure, but also offers an additional active material for Faradaic redox reaction in the electrode, which makes further improvement of the specific capacitance. Overall, the unique structure of the hierarchical $CoMoO_4/Co_3O_4$ nanohybrid gains a number of advantages that benefit supercapacitive energy storage devices.

3.5 Electrochemical performance of Asymmetric supercapacitor. To further explorer the electrochemical performance toward practical application of $CoMoO_4/Co_3O_4$, the asymmetric supercapacitor was fabricated by employing the as-synthesized $CoMoO_4/Co_3O_4$ and activated carbon (AC) as the positive and negative electrode in 3 M KOH with one piece of separator. Figure 8a shows the CV curves of CoMoO4/Co3O4 and AC electrode performed in three-electrode system. The AC electrode exhibits typical characteristic of electric double-layer capacitance within the range of −1.0 to 0 V, while the working voltage of the CoMoO4/Co3O4

electrode varies from -0.1 to 0.65 V. The working voltage of the asymmetric supercapacitor thus can be extended to 1.6 V, implying the potential of the assembled system in practical application.

Figure 8b exhibits the CV curves of the full cell within an operating voltage of 1.6 V. There is no obvious distortion of the CV curves with the scan rate ranging from 10 to 100 mV/s, indicating the favorable fast charge–discharge performance of the device. This unique charge–discharge property of the full cell is also demonstrated by the GCD curves displayed in Figure 8c, which presents nearly symmetric charge and discharge curves with no obvious internal voltage drops at different current densities. The calculated specific capacitance of the asymmetric supercapacitor based on total mass loading of the active materials is 124.5, 117.5, 97.25, 94.5 and 89 F/g at 1, 2, 4, 8 and 16 A/g, respectively. 71.5% of the initial capacitance is retained when the current density increases from 1 to 16 A/g. Furthermore, based on the GCD curves at different charge-discharge current density, an energy density of 44.27 Wh/kg is obtained at a power density of 637 W/kg. Most importantly, the energy density still remains at 31.64 Wh/kg when the power density increases to 7270 W/kg. This performance of our asymmetric supercapacitor is among the best devices from the previous literature.[16, 18, 21]

Besides, durable cyclic tolerance is a challenging issue for supercapacitor. The cyclic stability of the full cell was evaluated under repeated charging-discharging measurement at a constant current density of 16 A/g, as shown in Figure 8d. A gradually increase of specific capacitance at the initial 500 cycles is observed, this is

ascribed to the complete activation of the electrode. More significantly, the loss in specific capacitance based on the maximum value is only 0.38% after 2000 cycles, exhibiting excellent cycling stability. The results above demonstrate the as-prepared asymmetric supercapacitor based on CoMoO4/Co3O4 and AC is full of commercial application prospect.

4 CONCLUSIONS

In conclusion, the hierarchical $CoMoO_4/Co_3O_4$ nanocomposite was successfully fabricated via a one pot hydrothermal method followed by an annealing process. The growth mechanism of this hybrid nanostructure was rationalized based on the reaction time dependent experiments. Due to the unique 3D nanostructure, the hybrid sample displayed outstanding performance as electrode material in supercapacitors. A specific capacitance of 1062.5 F/g was obtained at the current densities of 1 A/g. After 2000 cycles with a current density of 20 A/g, 90.38% of the initial capacitance was maintained. After assembled to asymmetric supercapacitors, an energy density of 31.64 Wh/kg is achieved at the power density of 7270 W/kg. As a low cost electrode material with facile synthetic route and high electrochemical performance, the $CoMoO_4/Co_3O_4$ hybrid nanostructure in this work provides a promising candidate for the fabrication of supercapacitors.

Acknowledgements

The authors acknowledge the financial support provided by National Natural Science Fund of China (No. 61301026 and 51301152). We also appreciate the technical support from Testing Center of Yangzhou University.

Notes and references

College of Physical Science and Technology, and Institute of Optoelectronic Technology, Yangzhou University, Yangzhou 225002, People's Republic of China

Corresponding author* E-mail: xhzeng@yzu.edu.cn

Electronic Supplementary Information (ESI) available: [details of any supplementary information available should be included here]. See DOI: 10.1039/b000000x/

1 P. Simon and Y. Gogotsi, *Nat. Mater.*, 2008, **7**, 845-854.
2 J. R. Miller and P. Simon, *Science.*, 2008, **321**, 651-652.
3 H. Jiang, J. Ma and C. Li, *Chem.Commun.*, 2012, **48**, 4465-4467.
4 M. C. Liu, L. B. Kong, C. Lu, X. M. Li, Y. C. Luo and L. Kang, *ACS. Appl. Mater. Interfaces.*, 2012, **4**, 4631-4636.
5 C. O. Ania, V. Khomenko, E. Raymundo‐Piñero, J. B. Parra and F. Beguin, *Adv. Funct. Mater.*, 2007, **17**, 1828-1836.
6 C.-C. Hu, K.-H. Chang, M.-C. Lin and Y.-T. Wu, *Nano. Letters.*, 2006, **6**, 2690-2695.
7 B. E. Conway, *J. Electrochem. Soc.*, 1991, **138**, 1539-1548.
8 Q. Qu, P. Zhang, B. Wang, Y. Chen, S. Tian, Y. Wu and R. Holze, *J. Phys. Chem. C.*, 2009, **113**, 14020-14027.
9 C. Yuan, X. Zhang, L. Su, B. Gao and L. Shen, *J. Mater. Chem.*, 2009, **19**, 5772-5777.
10 W. Xiao, H. Xia, J. Y. H. Fuh and L. Lu, *J. Power. Sources.*, 2009, **193**, 935-938.
11 S. Xiong, C. Yuan, X. Zhang, B. Xi and Y. Qian, *Chem-Eur. J.*, 2009, **15**, 5320-5326.
12 W. Yu, X. Jiang, S. Ding and B. Q. Li, *J. Power. Sources.*, 2014, **256**, 440-448.
13 Y. Li, Z. Li and P. K. Shen, *Adv. Mater.*, 2013, **25**, 2474-2480.
14 X. Yu, B. Lu and Z. Xu, *Adv. Mater.*, 2014, **26**, 1044-1051.
15 H. Chen, J. Jiang, L. Zhang, H. Wan, T. Qi and D. Xia, *Nanoscale.*, 2013, **5**, 8879-8883.
16 X. Xia, W. Lei, Q. Hao, W. Wang and X. Wang, *Electrochim. Acta.*, 2013, **99**, 253-261.
17 M.-C. Liu, L.-B. Kong, C. Lu, X.-M. Li, Y.-C. Luo and L. Kang, *Mater. Lett.*, 2013, **94**, 197-200.
18 L. Q. Mai, F. Yang, Y. L. Zhao, X. Xu, L. Xu and Y. Z. Luo, *Nat. Commun.*, 2011, **2**, 381.
19 X.-J. Ma, L.-B. Kong, W.-B. Zhang, M.-C. Liu, Y.-C. Luo and L. Kang, *Electrochim. Acta.*, 2014, **130**, 660-669.
20 R. Ramkumar, M. Minakshi, *Dalton. Trans*, 2015, **44**, 6158-6168.
21 Z. Gu, H. Nan and B. Geng, *J. Mater. Chem. A.*, 2015, **3**, 14578-14584.
22 M. Zhou, F. Lu, T. Lv, X. Yang, W. Xia, X. Shen, H. He and X. Zeng, *J. Phys. D. Appl. Phys.*, 2015, **48**, 215305.
23 T. He, D. Chen, X. Jiao, Y. Wang and Y. Duan, *Chem. Mater.*, 2005, **17**, 4023-4030.
24 R. Xu and H. C. Zeng, *The J. Phys. Chem. B.*, 2003, **107**, 12643-12649.

25 G. Kianpour, M. Salavati-Niasari and H. Emadi, *Superlattice. Microst.*, 2013, **58**, 120-129.
26 M. Mandal, D. Ghosh, S. Giri, I. Shakir and C. K. Das, *RSC. Adv.*, 2014, **4**, 30832.
27 J. Zhang, P. Li, Z. Wang, J. Qiao, D. Rooney, W. Sun and K. Sun, *J. Mater. Chem. A.*, 2015, **3**, 1504-1510.
28 C. T. Cherian, M. V. Reddy, S. C. Haur and B. V. Chowdari, *ACS. Appl. Mater. Interfaces.*, 2013, **5**, 918-923.
29 S. Baskar, D. Meyrick, K. S. Ramakrishnan and M. Minakshi, *Chem. Eng. J.*, 2014, **253**, 502-507.
30 H. Li, Y. Gao, C. Wang and G. Yang, *Adv. Energy. Mater.*, 2015, **5**, doi: 10.1002/aenm.201401767.
31 Y. Ding, Y. Wan, Y.-L. Min, W. Zhang and S.-H. Yu, *Inorg. Chem.*, 2008, **47**, 7813-7823.
32 K. Eda, Y. Uno, N. Nagai, N. Sotani and M. Stanley Whittingham, *J. Solid. State. Chem.*, 2005, **178**, 2791-2797.
33 R. Candia, B. S. Clausen and H. Topsøe, *Bull. Soc. Chim. Belg.*, 1981, **90**, 1225-1232.
34 S.-C. Wang and W.-C. J. Wei, *Nanostruct. Mater.*, 1998, **10**, 983-1000.
35 W. H. R. Shaw and J. J. Bordeaux, *J. Am. Chem. Soc.*, 1955, **77**, 4729-4733.
36 L. Zhu, Z. Wen, W. Mei, Y. Li and Z. Ye, *The J. Phys. Chem. C.*, 2013, **117**, 20465-20473.
37 Y. Zhang, M. Ma, J. Yang, H. Su, W. Huang and X. Dong, *Nanoscale.*, 2014, **6**, 4303-4308.
38 D. Guo, H. Zhang, X. Yu, M. Zhang, P. Zhang, Q. Li and T. Wang, *J. Mater. Chem. A.*, 2013, **1**, 7247.
39 C. Yuan, J. Li, L. Hou, X. Zhang, L. Shen and X. W. D. Lou, *Adv. Funct. Mater.*, 2012, **22**, 4592-4597.
40 D. Ghosh, S. Giri and C. K. Das, *Nanoscale.*, 2013, **5**, 10428-10437.
41 W. Kang, Y. Tang, W. Li, X. Yang, H. Xue, Q. Yang and C. S. Lee, *Nanoscale.*, 2015, **7**, 225-231.
42 D. Cai, B. Liu, D. Wang, Y. Liu, L. Wang, H. Li, Y. Wang, C. Wang, Q. Li and T. Wang, *Electrochim. Acta.*, 2014, **115**, 358-363.

Figures and figure captions

Fig 1. FESEM and TEM images of the as-prepared 3D hybrid hierarchical precursor (a, c) and the annealed sample transformed from the precursor (b, d). The insets in a and b are the magnified images of each sample.

Fig 2. XRD patterns of the annealed sample (a) and the precursor sample before annealing (b), FTIR spectroscopy (c) of the annealed sample and the precursor sample, Raman spectroscopy of the annealed sample (d) and the precursor sample (e), and N_2 adsorption–desorption isotherm of the annealed sample (f) and the precursor (g). The pore size distribution labeled as inset obtained from adsorption branches by BJH method.

Fig 3. Schematic illustration of the formation process of the precursor (a-d). SEM images of the time-dependent intermediate products obtained at 30 min (e), 60 min (f), 90 min (g) and 120 min (h). XRD patterns of the intermediate products (i-l). Stage 1, the $CoMoO_4$ nanorods are synthesized. Stage 2, the formation of $Co(CO_3)_{0.5}(OH)\cdot 0.11H_2O$ framework accompanied by the dissolution of $CoMoO_4$ nanorods in ammonia. Stage 3, the precursor of $CoMoO_4$ nanosheets in-suit grow on the skeleton. Stage 4, the formation of the final nanohybrid with 3D nanostructure.

Fig 4. HRTEM images of the nanosheet (b) and nanorod (c) separated from the annealed sample (a), and SAED pattern of the annealed sample (d).

Fig 5. Electrochemical measurments of the annealed sample. Cyclic voltammetry (CV) of $CoMoO_4/Co_3O_4$ at various scan rates (a), galvanostatic charge-discharge (GCD) curves at different current densities (b), cylic performace of the annealed sample (c), and electrochemical impedance spectra of the annealed sample after the 1st and 2000th cycle (d).

Fig 6. Electrochemical measurments of the precursor. Cyclic voltammetry (CV) curves of the precursor (a) at various scan rates, galvanostatic charge-discharge (GCD) curves (b) at different current densities, and the cylic performace of the precursor (c).

Fig 7. Cyclic voltammetry (CV) curves of sample S21, sample S11 and sample S12 at 100 mV/s (a), galvanostatic charge-discharge (GCD) curves of sample S21, sample S11 and sample S12 at the current density of 1 A/g.

Fig 8. Electrochemical measurments of the asymmetric supercapacitor. Cyclic voltammetry (CV) curves of the $CoMoO_4/Co_3O_4$ and active carbon as working electrodes in three-electrode system (a), Cyclic voltammetry (CV) curves of the asymmetric supercapacitor at various scan rates (b), galvanostatic charge-discharge (GCD) curves of the asymmetric supercapacitor at different current densities (c), and cylic performace of the asymmetric supercapacitor (d).

Fig 1

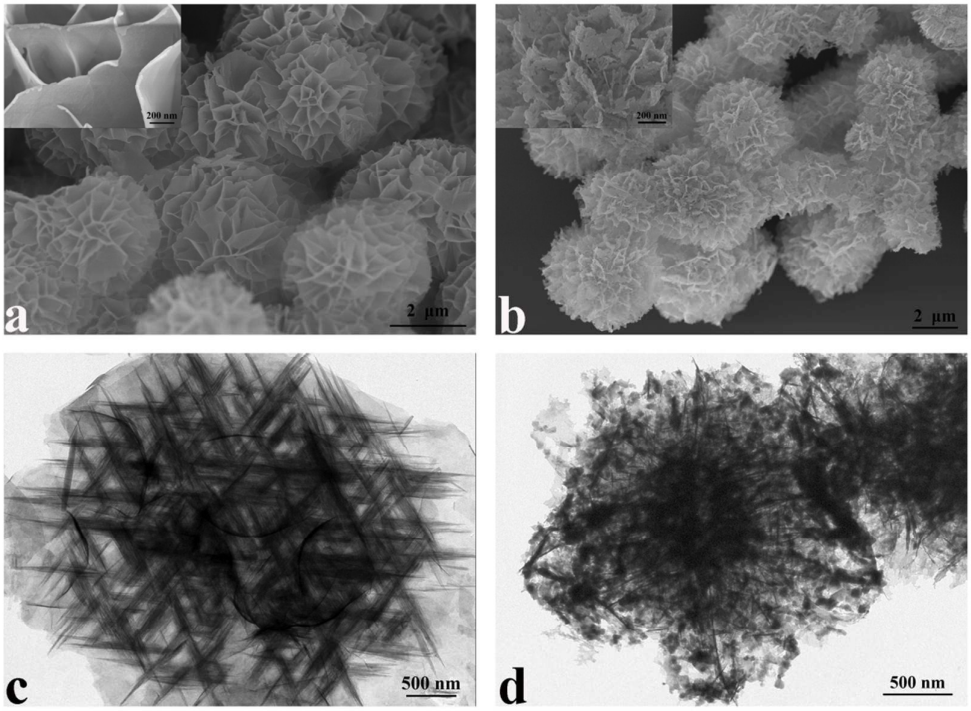

Fig 2

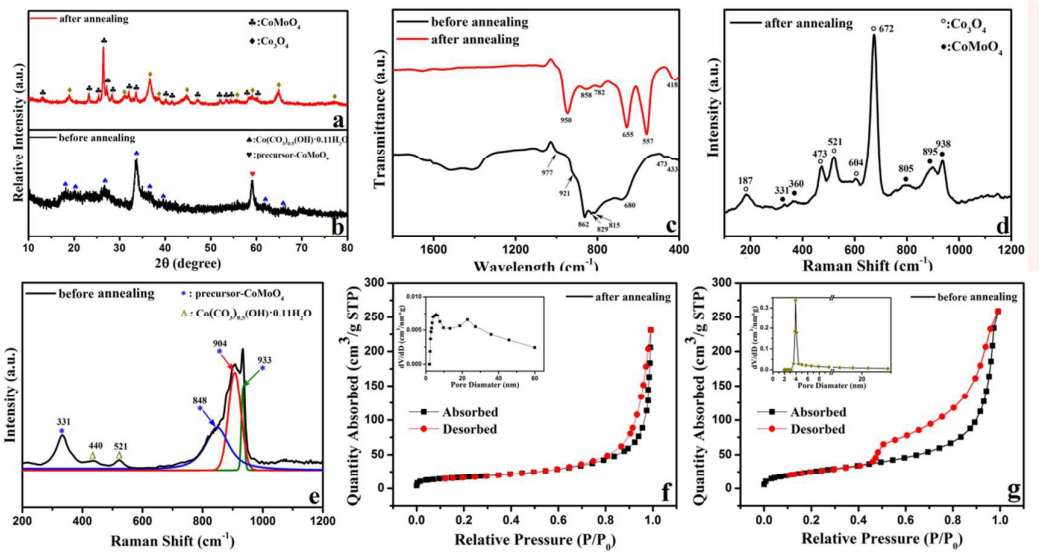

Fig 3

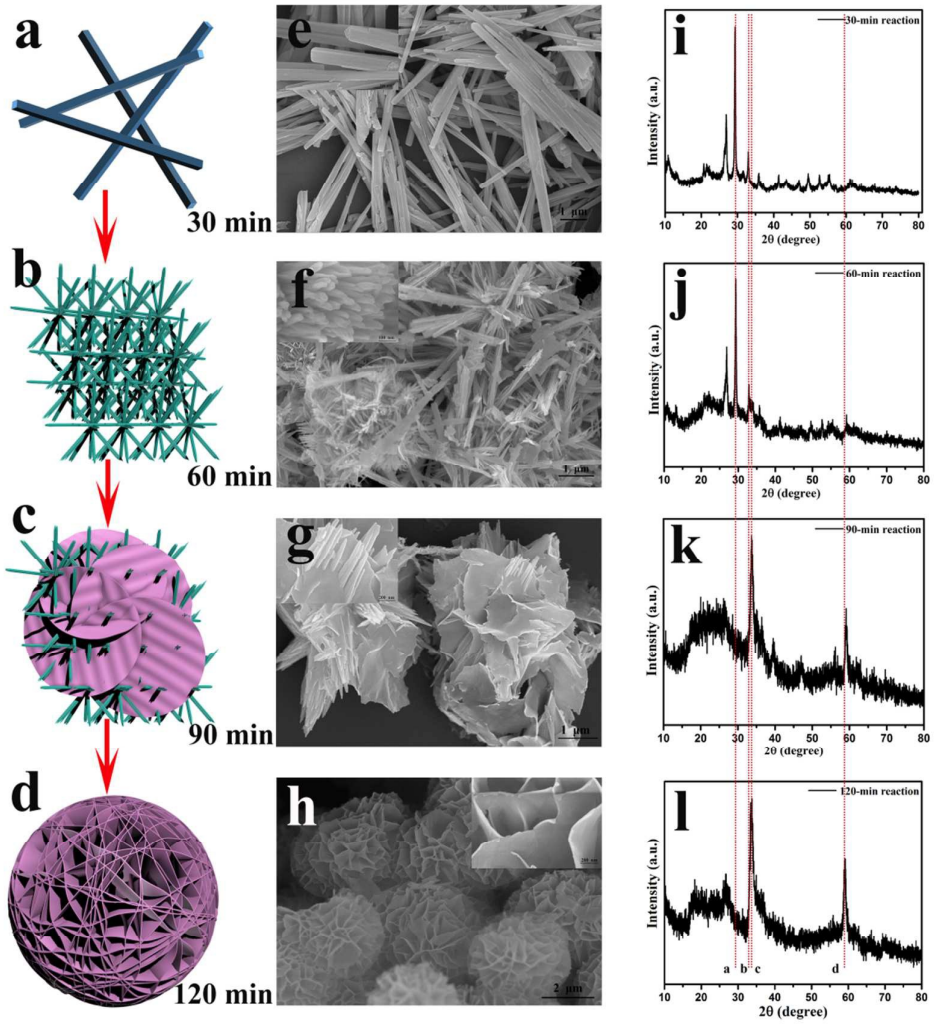

Fig 4

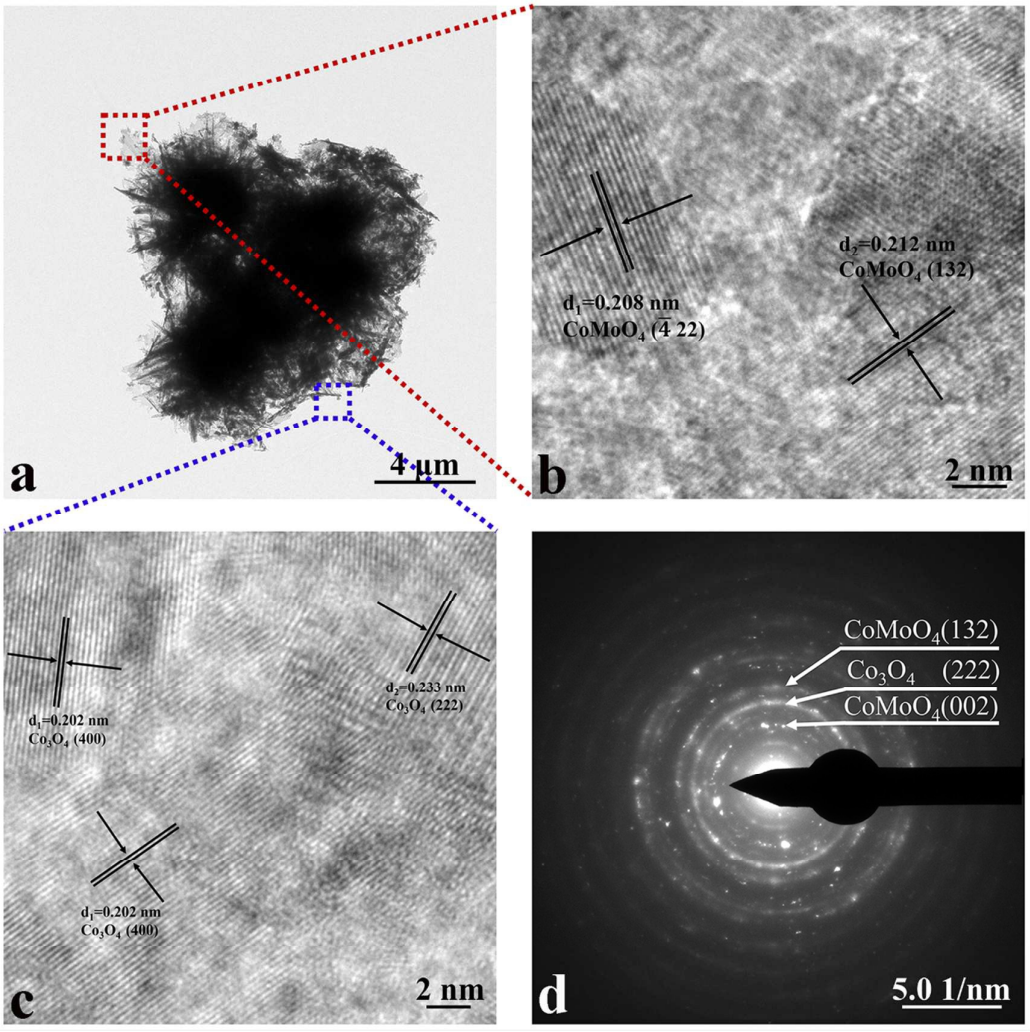

Fig 5

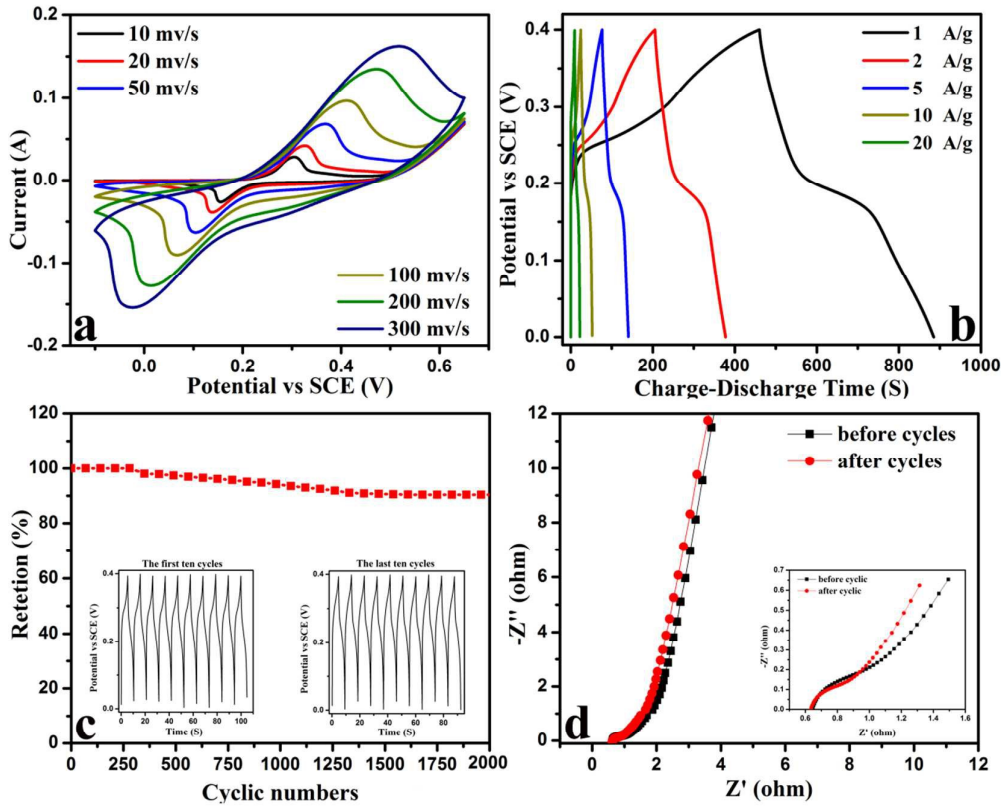

Fig 6

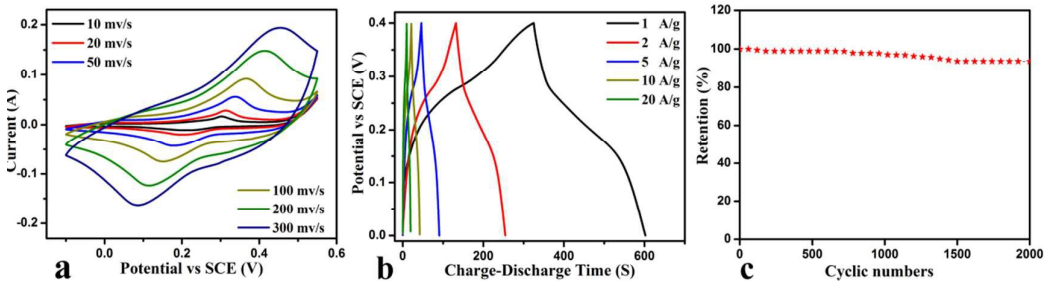

Fig 7

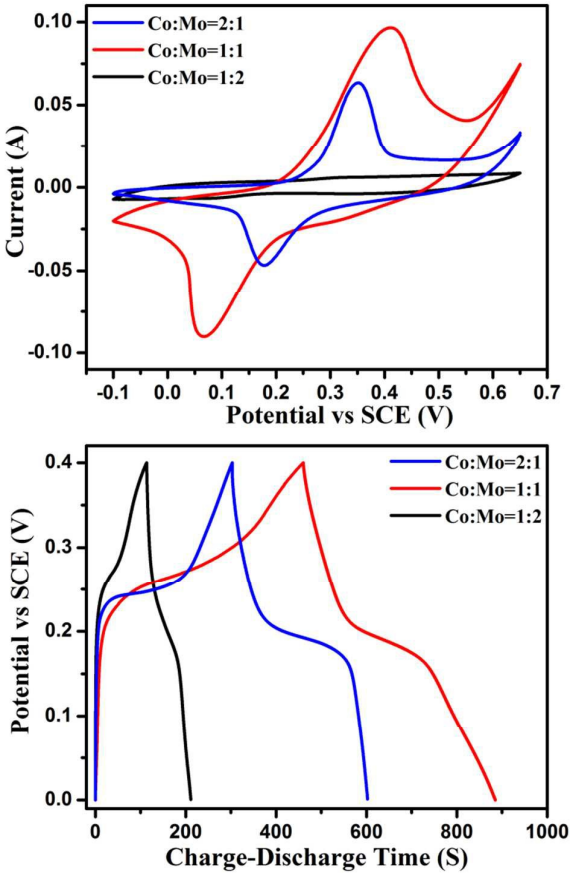

Fig 8

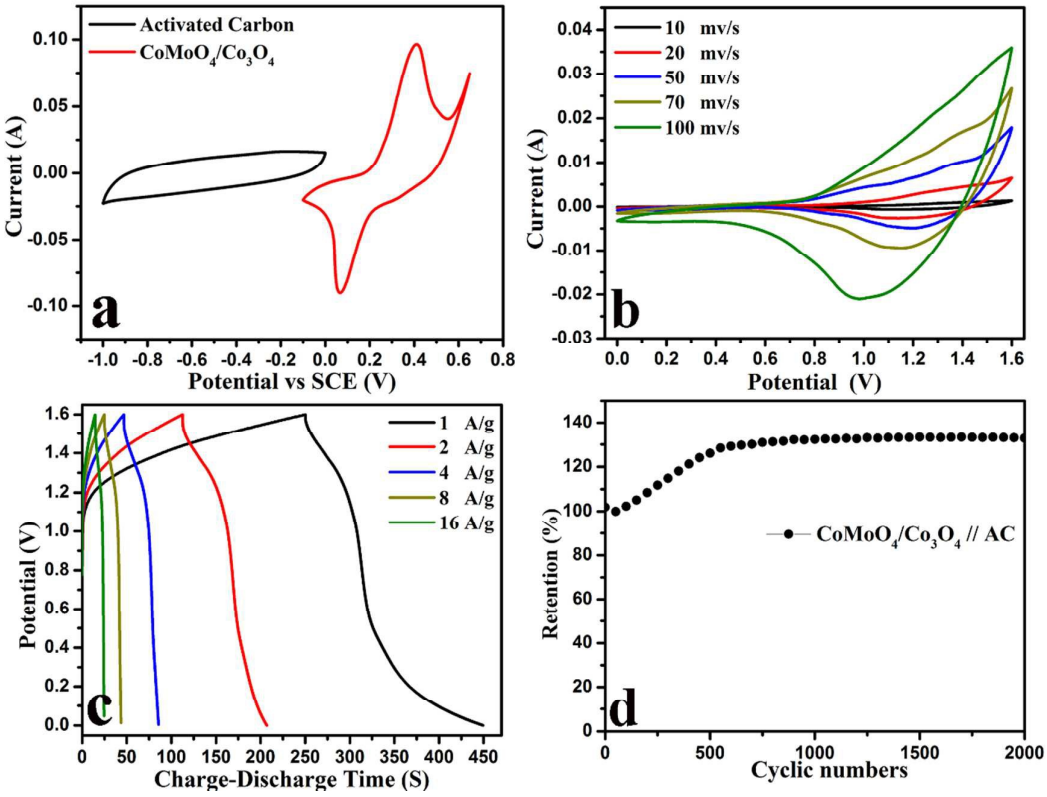

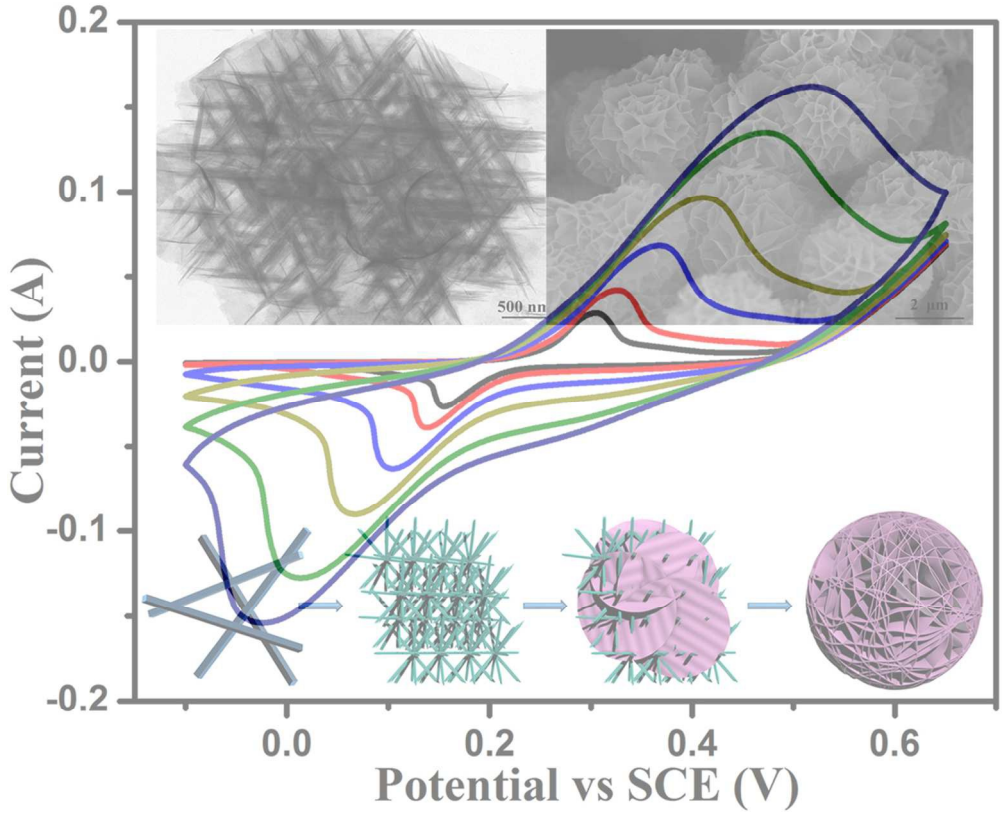

Three dimensional CoMoO4/Co3O4 hybrid nanostructures were synthesized via one-pot hydrothermal method and displayed excellent performance as electrode material in supercapacitors
101x83mm (300 x 300 DPI)